



# Research Repository UCD

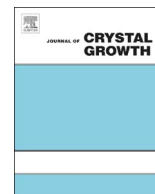
<b>Title</b>	Direct observation of spatially isothermal equiaxed solidification of an Al-Cu alloy in microgravity on board the MASER 13 sounding rocket
<b>Authors(s)</b>	Murphy, A. G., Mathiesen, Ragnvald H., Browne, David J., et al.
<b>Publication date</b>	2016-11-15
<b>Publication information</b>	Murphy, A. G., Ragnvald H. Mathiesen, David J. Browne, and et al. "Direct Observation of Spatially Isothermal Equiaxed Solidification of an Al-Cu Alloy in Microgravity on Board the MASER 13 Sounding Rocket." Elsevier, November 15, 2016. <a href="https://doi.org/10.1016/j.jcrysgro.2016.08.054">https://doi.org/10.1016/j.jcrysgro.2016.08.054</a> .
<b>Publisher</b>	Elsevier
<b>Item record/more information</b>	<a href="http://hdl.handle.net/10197/8241">http://hdl.handle.net/10197/8241</a>
<b>Publisher's version (DOI)</b>	<a href="https://doi.org/10.1016/j.jcrysgro.2016.08.054">10.1016/j.jcrysgro.2016.08.054</a>

Downloaded 2025-12-04 22:54:47

The UCD community has made this article openly available. Please share how this access benefits you. Your story matters! (@ucd\_oa)



© Some rights reserved. For more information



# Direct observation of spatially isothermal equiaxed solidification of an Al–Cu alloy in microgravity on board the MASER 13 sounding rocket



A.G. Murphy<sup>a</sup>, R.H. Mathiesen<sup>b</sup>, Y. Houltz<sup>c</sup>, J. Li<sup>c</sup>, C. Lockowandt<sup>c</sup>, K. Henriksson<sup>c</sup>,  
N. Melville<sup>d</sup>, D.J. Browne<sup>a,\*</sup>

<sup>a</sup> School of Mechanical and Materials Engineering, University College Dublin, Belfield, Dublin 4, Ireland

<sup>b</sup> Department of Physics, Norwegian University of Science and Technology, N-7491 Trondheim, Norway

<sup>c</sup> Swedish Space Corporation (SSC), P.O. Box 4207, SE-171 04 Solna, Sweden

<sup>d</sup> European Space Agency, European Space Research & Technology Centre (ESTEC), Keplerlaan 1 Postbus 299, 2200 AG Noordwijk, The Netherlands

## ARTICLE INFO

### Article history:

Received 29 April 2016

Received in revised form

9 August 2016

Accepted 28 August 2016

Communicated by: T.F. Kuech

Available online 3 September 2016

### Keywords:

A1. Dendrites, Solidification

A2. Microgravity conditions

B1. Alloys

## ABSTRACT

For the first time, isothermal equiaxed solidification of a metallic alloy has been observed in situ in space, providing unique benchmark experimental data. The experiment was completed on board the MASER 13 sounding rocket, launched in December 2015, using a newly developed isothermal solidification furnace. A grain-refined Al–20 wt%Cu sample was fully melted and solidified during 360 s of microgravity and the solidification sequence was recorded using time-resolved X-radiography. Equiaxed nucleation, dendritic growth, solutal impingement, and eutectic transformation were thus observed in a gravity-free environment.

Equiaxed nucleation was promoted through application of a controlled cooling rate of  $-0.05$  K/s producing a 1D grain density of  $\sim 6.5 \text{ mm}^{-1}$ , uniformly distributed throughout the field of view (FOV). Primary growth slowed to a visually imperceptible level at an estimated undercooling of 7 K, after which the cooling rate was increased to  $-1.0$  K/s for the remainder of solidification and eutectic transformation, ensuring the sample was fully solidified inside the microgravity time window. The eutectic transformation commenced at the centre of the FOV proceeding radially outwards covering the entire FOV in  $\sim 3$  s.

Microgravity-based solidification is compared to an identical pre-flight ground-based experiment using the same sample and experiment timeline. The ground experiment was designed to minimise gravity effects, by choice of a horizontal orientation for the sample, so that any differences would be subtle. The first equiaxed nucleation occurred at an apparent undercooling of 0.6 K less than the equivalent event during microgravity. During primary equiaxed solidification, as expected, no buoyant grain motion was observed during microgravity, compared to modest grain rotation and reorientation observed during terrestrial-based solidification. However, when the cooling rate was increased from  $-0.05$  K/s to  $-1.0$  K/s during the latter stages of solidification, in both 1g and micro-g environments, some grain movement was apparent due to liquid feeding and mechanical impingement of neighbouring grains.

© 2016 The Authors. Published by Elsevier B.V. This is an open access article under the CC BY-NC-ND license (<http://creativecommons.org/licenses/by-nc-nd/4.0/>).

## 1. Introduction

Gravity can play a significant role during solidification, leading to segregation and other casting defects normally associated with liquid metal processing [1]. Furthermore, liquid–solid motion as a result of gravity-induced buoyant flow is a significant complication in computational simulations of solidification, leading to long simulation times [2]. Sophisticated mathematical and

computational models of solidification require experimental validation. *In situ* X-radiography of solidification has, in recent times [3,4], enabled observations of dynamic solidification phenomena in real time, allowing direct comparison with both numerical [5,6] and mathematical [7–10] predictions. To reduce complexity, it is desirable to eliminate gravity effects during solidification in both numerical models and related benchmark experiments. While it is a simple matter to ‘switch off’ gravity in a computer simulation, eliminating gravity during solidification experiments is more challenging. However, the advent of compact in situ X-ray diagnostics [11], combined with sophisticated furnace designs [8,12,13], has allowed solidification to be performed on board

\* Corresponding author.

E-mail address: [david.browne@ucd.ie](mailto:david.browne@ucd.ie) (D.J. Browne).

short duration microgravity platforms such as Sounding Rockets [12] and on board Parabolic Flight Campaigns [14].

Microgravity has been used for solidification experiments, in conjunction with both *in situ* and *ex situ* analysis, for several decades. Glicksman et al. [15] performed isothermal solidification of a transparent material, on board the Columbia Space Shuttle (STS-62), using the Isothermal Dendritic Growth Experiment (IDGE) apparatus in conjunction with pure succinonitrile (SCN) and *in situ* optical microscopy. Dhindaw et al. [16] performed directional solidification of monotectic alloys on board a Parabolic Flight using a Bridgman-type gradient furnace and *ex situ* post-flight metallographic analysis. Directional solidification of Al–Si on board Sounding Rockets and the International Space Station (ISS) has also been performed [17,18].

More recently, Nguyen-Thi et al. [12,19] performed a directional solidification experiment on board the MASER 12 Sounding Rocket, launched in February 2012, using the purpose-built Bridgman-style XRMON Gradient Furnace (GF) and an Al–20 wt% Cu sample strip. The MASER 12 solidification experiment successfully demonstrated the feasibility of performing solidification in microgravity on board sounding rockets, in conjunction with high resolution *in situ* X-ray diagnostics, allowing for direct comparison of terrestrial and microgravity solidification. Murphy et al. [14] performed near-isothermal equiaxed solidification using a grain refined (GR) Al–20 wt%Cu sample, also using the XRMON-GF, on board a parabolic flight campaign. Isothermal conditions were achieved by setting a flat temperature profile across the sample and cooling both heaters at the same rate to promote solidification. Critically, during post-flight analysis, it was noted that free growing equiaxed grains were sensitive to g-level fluctuations during the flight. This was due to the relatively low quality microgravity available on board parabolic flight campaigns, i.e.  $\pm 0.05g$ . Due to practical and safety constraints on the manned flight, in a commercial aircraft, only 21 s of continuous microgravity time is achieved during the parabolic flight, and each such period is sandwiched between hyper-gravity periods [20]. Furthermore, the use of a gradient furnace in ‘isothermal-mode’ provided sub-optimal isothermal solidification conditions [7]. The importance of the orientation of the thin sample with respect to the gravity vector, on earth, has been demonstrated in XRMON-GF experiments on equiaxed solidification. We showed [7] that a dramatic difference occurs between experiments in which the sample is vertical and those in which it is horizontal. For the latter situation, buoyancy effects are limited to acting in the thin sample direction and are constrained by the top and bottom crucible surfaces, which are only 200  $\mu\text{m}$  apart. With the success of XRMON-GF on board MASER 12, a dedicated isothermal furnace, XRMON-SOL [8], was commissioned by the European Space Agency, and scheduled for flight on board the MASER 13 sounding rocket. About 6 min of microgravity time is available on this platform. For the reasons just outlined, the performance of XRMON-SOL was initially tested [8] on earth in a configuration in which the samples were horizontal.

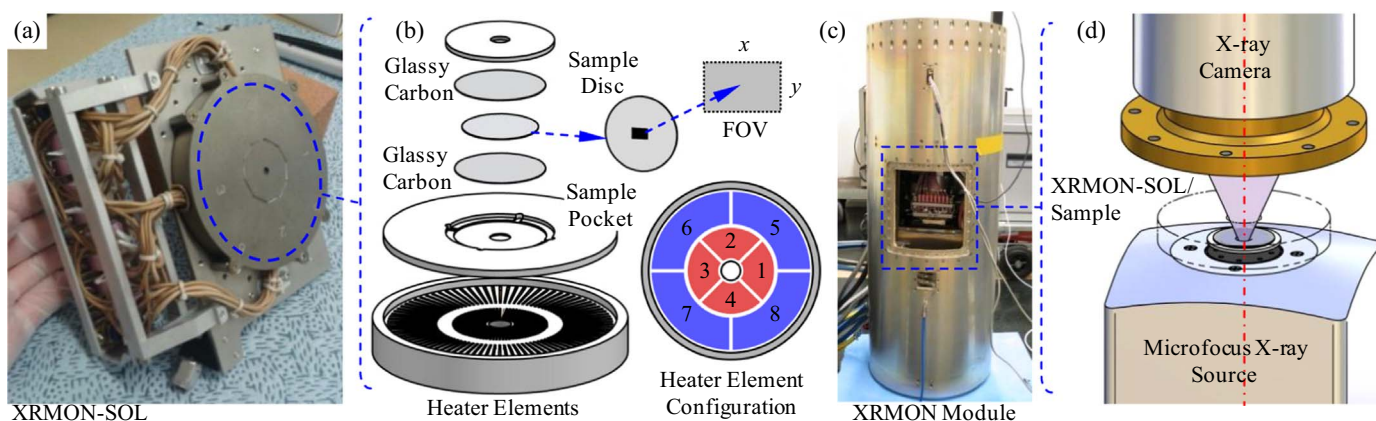
This work presents the first dedicated isothermal solidification microgravity-based solidification experiment performed using the XRMON-SOL. Details of the experimental configuration and the experiment timeline are presented along with an overview of the results observed *in situ*, i.e. equiaxed and eutectic solidification. Microgravity-based solidification measurements are compared with identical experiments performed using the same experimental configuration under terrestrial conditions to determine the implications of microgravity vs. terrestrial solidification experiments.

## 2. Experimental

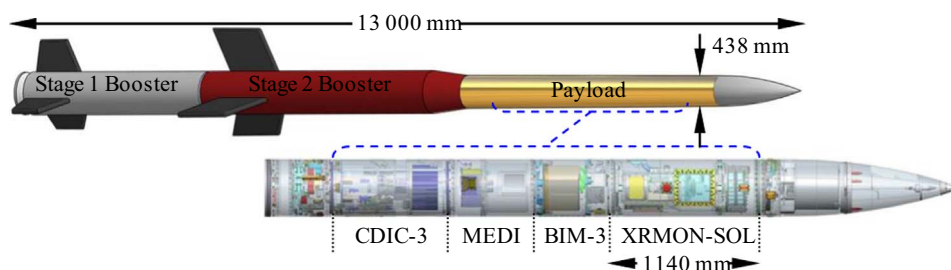
XRMON-SOL is a newly developed isothermal solidification furnace designed specifically to operate under microgravity and terrestrial conditions, in conjunction with high resolution *in situ* X-ray diagnostics. The compact nature of both the furnace and the X-ray diagnostics allows for real time imaging of alloy solidification on board microgravity platforms, such as sounding rockets, parabolic flights and the International Space Station, as well as in ground-based home laboratories. XRMON-SOL was selected to fly on board the MASER 13 sounding rocket with the goal of performing isothermal equiaxed solidification of a grain refined Al–20 wt%Cu alloy in the absence of any buoyancy or convection effects normally associated with terrestrial solidification e.g. during casting. A full description of the XRMON-SOL has already been provided [8], thus only a brief outline of pertinent features and functions will be provided herein.

Fig. 1(a) shows the flight model XRMON-SOL prior to installation within the XRMON module on board the MASER 13 Sounding Rocket. The outer metallic housing and mounting framework encases the inner furnace body, shown in Fig. 1(b). The furnace body comprises a boron-nitride monoblock, into which eight independent heater coils are wound, along with eight embedded regulating/monitoring k-type thermocouples. A sample alloy disc, measuring 21 mm in diameter and 200  $\mu\text{m}$  thick is sandwiched between two glassy carbon discs and positioned in a boron-nitride sample pocket, which is in direct contact with the heater elements. All the individual components are clamped together by the insulated housing lid, highlighted in Fig. 1(a), ensuring good thermal contact and a fast thermal response between the heater control system and the real time *in situ* observations. The X-ray field of view (FOV) is coincident with the sample centre measuring approximately  $4.1 \times 2.8$  mm (FOV x- and y-axes, respectively), with a spatial resolution of  $\sim 6.1 \mu\text{m}$  [11]. The eight heater elements are configured, as shown in Fig. 1(b), into two concentric heater rings segmented into four independently regulated zones, allowing for fine adjustment of the temperature field throughout the observable FOV. The XRMON module, shown in Fig. 1(c), houses the *in situ* X-ray diagnostics, on board furnace control system, and memory. The X-ray diagnostics comprised a 3  $\mu\text{m}$  microfocus X-ray source and a structured X-ray scintillator equipped 10 megapixel CCD camera, Fig. 1(d). A full description of the X-ray equipment used in this work has already been described in detail elsewhere [8,11,12]. Optimal image contrast during solidification was achieved using X-ray source settings of 50 keV and 60  $\mu\text{A}$ . Images were recorded on board the XRMON module at a rate of 3 Hz. During the MASER 13 flight, images were relayed in real time to the ground support monitoring station at a rate of 1 Hz, thereby allowing operator override of the automated experiment sequence in the event of any unforeseen anomalies. Ultimately, however, no operator intervention was required during the microgravity window, with successful melting and solidification of the sample achieved prior to the cessation of microgravity conditions.

The alloy system chosen for study was Al–20 wt%Cu grain refined (GR) with industrial grade  $< 0.1$  wt%Al–Ti–B(5/1) master alloy. The relatively high hypoeutectic copper concentration was selected to provide high image contrast during solidification, with copper atoms providing higher attenuation of the incident X-ray beam than aluminium atoms [21]. Thus, within the FOV during solidification, solid  $\alpha$ -Al equiaxed crystals appear brighter than the surrounding copper rich Al–Cu liquid, with contrast increasing throughout solidification due to continued solute partitioning. Samples were produced by casting approximately 75g (combined mass) of 6N purity aluminium and 3N purity copper, along with the industrial GR, into a cylindrical steel mould to promote a relatively rapid solidification time, i.e. approximately 2 s, thereby



**Fig. 1.** (a) Flight model XRMON-SOL prior to installation in the XRMON module on board the MASER 13 Sounding Rocket. (a) Exploded view of the internal XRMON-SOL furnace assembly showing the encasement of the sample disc ( $\phi$  21.0  $\times$  0.2 mm) between two glassy carbon discs and then sealed within a boron-nitride pocket mounted on top of the heater elements. Labels 1–8 of the Heater Element Configuration indicate the relative location and arrangement of the eight independently regulated heater coils. The field-of-view (FOV) x-axis and y-axis represent the physical extent of the X-ray field-of-view relative to the sample diameter, horizontally ( $\sim$ 4.1 mm) and vertically ( $\sim$ 2.7 mm), respectively. (c) XRMON module with XRMON-SOL installed, prior to integration on board the MASER 13 Sounding Rocket. (d) *In situ* X-ray diagnostics configuration inside the XRMON module, comprising a microfocus X-ray source and X-ray camera mounted inline with the module/rocket axis.



**Fig. 2.** Schematic illustration of the fully assembled MASER 13 Sounding Rocket, consisting of two booster rocket stages, the payload assembly, and finally the nose cone/recovery system. The scientific experiment payload comprised four separate experiments, with the XRMON module mounted at the front, behind the nose cone/recovery system.

minimising segregation within the casting volume. Sample discs were thereafter sectioned from the cast ingot and then manually ground to a thickness of 200  $\mu$ m, and polished to a surface roughness of 1  $\mu$ m. A more complete and detailed description of the sample manufacturing process developed for this work can be found in Ref. [22]. Several sample discs were produced for the MASER 13 flight, however a single sample was used for both the ground-based reference experiment, performed prior to the launch, and the microgravity flight on board the MASER 13 Sounding Rocket. Due to the practical constraints of a sounding rocket campaign, such as MASER 13, only one microgravity solidification experiment could be performed. The best way to assess the effects of gravity is to compare the exact same sample in the same furnace – solidified in 1g and micro-g. The 1g experiment had to be performed prior to the rocket flight, because of likely damage to the experimental equipment on landing – this proved to be the case. Excessive runs on ground prior to flight could also lead to deterioration of sample or furnace, so this was avoided. However the performance of XRMON-SOL in terrestrial experiments has been well characterised in previous work [8].

The MASER 13 (Material Science Experiment Rocket) is a sub-orbital microgravity research rocket that was launched by the Swedish Space Corporation from Esrange in northern Sweden at 6:00 a.m. local time on December 1st, 2015. MASER-type Sounding Rockets can provide between 6 and 7 min of high quality microgravity, i.e.  $< 10^{-4}$ g, depending on weather conditions. MASER 13 achieved microgravity conditions approximately  $t=90$  s after launch, reaching an apogee of 262 km at time  $t=240$  s, with restoration of positive g, i.e.  $\geq 1$ g, at  $t=442$  s, ultimately achieving slightly less than 6 min of microgravity. Fig. 2 schematically

illustrates the MASER rocket configuration consisting of two booster rocket stages, onto which the payload is mounted, along with the recovery system and nose cone. The experiment payload for MASER 13 consisted of four separate experiment modules, with the XRMON module mounted at the front. The XRMON module measured 1140 mm in length with a diameter of 438 mm and a mass of 99 kg, making it the largest/heaviest module on board MASER 13. Approximately 11 min after launch the MASER 13 payload achieved a parachute assisted crash-down in the target area  $\sim 70$  km north-west of the launch site, after which the payload was recovered and returned to the launch site.

A solidification experiment timeline was chosen to ensure that the sample was both melted and solidified completely within the microgravity window, thereby avoiding any hypergravity influence on the sample during lift-off or atmospheric re-entry. Fig. 3 shows the experiment timeline chosen for both microgravity-based solidification and ground-based solidification. Fifteen minutes ( $t = -900$  s) prior to launch the furnace temperature was raised to 540  $^{\circ}$ C, i.e. below the sample melting temperature, to both thermally stabilise the furnace/housing, and reduce time taken to fully melt the sample at the maximum achievable heating rate of 2 K/s. At  $t=60$  s, the automated flight sequence commenced heating of the furnace at a rate of 2 K/s up to 650  $^{\circ}$ C thereby completely melting the Al–Cu sample. Through extensive ground-based pre-flight testing, melting of the sample was fixed to commence approximately 3 s after microgravity conditions had been established. The sample was then held at 650  $^{\circ}$ C for 20 s, subsequently cooled to 625  $^{\circ}$ C at a rate of  $-1$  K/s and held for a further 20 s, after which time the primary solidification cooling rate of  $-0.05$  K/s was applied to all eight heaters simultaneously. Note



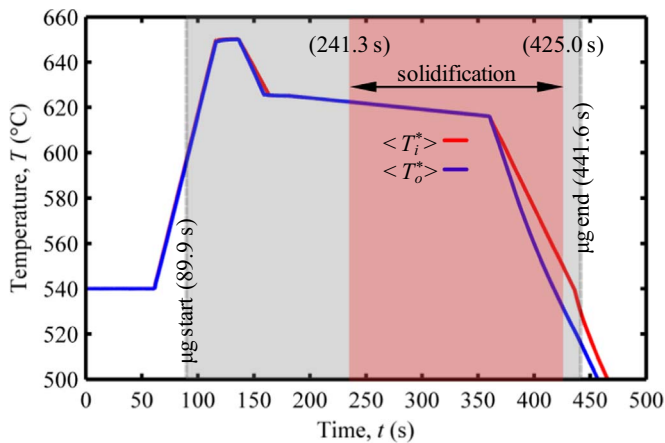


**Fig. 3.** MASER 13 and ground-based reference experiment timeline. Grey region shows microgravity period. Highlighted region (solidification) denotes period in which equiaxed nucleation, growth, and the eutectic transformation occurred. Time,  $t=0$  is the MASER 13 rocket launch time.  $\langle T_i \rangle$  and  $\langle T_o \rangle$  refer to the average measured inner and outer heater ring temperatures, respectively.

typically equiaxed grains only become visible in the FOV after they have increased in diameter to approximately  $50\ \mu\text{m}$ , after which time sufficient solid has formed to provide detectable solid–liquid contrast within the FOV. Equiaxed nucleation takes place at some time prior to the associated solid becoming visible [8]; thus the holding temperature was selected such that nucleation would not occur until a constant cooling rate of  $-0.05\ \text{K/s}$  had been applied. At time  $t=359\ \text{s}$ , and for the final stages of solidification, i.e. the eutectic transformation, the cooling rate was increased to  $-1\ \text{K/s}$  and  $-1.5\ \text{K/s}$  on the inner and outer heater rings, respectively, as shown in Fig. 3. Observable solidification within the FOV occurred between  $t=241$  and  $t=425\ \text{s}$ , indicated by the highlighted region in Fig. 3, with the sample returning to the fully solid state approximately 17 s prior to the cessation of microgravity conditions.

### 3. Results and Discussion

Both ground-based solidification and microgravity-based solidification experiments were successfully performed using the timeline shown in Fig. 3, with equiaxed nucleation and the subsequent eutectic transformation occurring within the microgravity window of  $t=90\text{--}442\ \text{s}$ . Fig. 4 shows a direct comparison of the time/temperature synced in situ microgravity ( $\mu\text{g}$ ) and terrestrial ( $1\text{g}$ ) observations, separated into column I and II, respectively. The full video sequence is also provided in Video 1. Tables 1 and 2 show the position, time, and furnace temperature at the time of each individual grain nucleation event. Note, as mentioned previously, direct observation of equiaxed nucleation was not possible with the current setup due to the poor image contrast provided by grains smaller than  $\sim 50\ \mu\text{m}$  in diameter. However, for the purposes of this preliminary investigation equiaxed nucleation will be defined as the time at which grains became detectable within the FOV.

Close inspection of the sequence images in Fig. 4 reveals no significant morphological differences between equiaxed solidification under microgravity and terrestrial conditions. After initial nucleation of several grains, equiaxed nucleation continued until the entire FOV was filled with randomly oriented, uniformly distributed equiaxed grains. Interestingly, as shown in Tables 1 and 2, equiaxed nucleation in microgravity commenced approximately 13 s earlier than observed during terrestrial solidification, at  $t=241\ \text{s}$  and  $254\ \text{s}$ , respectively. However, in both cases the first grain to nucleate was located in the NW corner of the FOV,

suggesting nucleation may have occurred on the same inoculant particle in both cases. The earlier nucleation observed in microgravity may be due to the absence of gravity during solidification. However, it may also be due to a reorientation of the inoculant particle into a more favourable position requiring less undercooling to nucleate, in this case  $\sim 0.65\ \text{K}$  less. For both microgravity and terrestrial solidification, nucleation was complete at  $t \approx 294\ \text{s}$  with a total of 22 grains and 23 grains nucleated within the FOV, respectively. As primary solidification continued, the intergranular liquid space between grains reduced to approximately the same level in both cases, as shown in Fig. 4(c). Finally, the eutectic transformation commenced at precisely the same time/temperature for both microgravity and terrestrial solidification at time  $t=414\ \text{s}$ . Fig. 4(d) shows the advancing eutectic transformation (dark shaded region) for microgravity and terrestrial solidification, column I and II, respectively. To more clearly show the eutectic transformation, the equiaxed microstructure was removed using post-processing image enhancement as described previously by Murphy et al. [23]. During microgravity-based solidification a single eutectic zone appeared within the FOV, whereas under terrestrial conditions two eutectic zones were observed to occur within the FOV. Thus, with each observed eutectic zone being approximately equal in size, the eutectic fraction at the time shown in Fig. 4(d) was approximately double for terrestrial solidification when compared to microgravity solidification. Interestingly, however, in both cases, the eutectic transformation within the FOV was complete at approximately the same time, i.e.  $t=425\ \text{s}$ . The fact that the eutectic zones originated within the FOV, and their growth was quite spatially uniform, also provides confidence that the thermal gradient is low in the region of interest.

Critically, the most significant difference observed between microgravity and terrestrial solidification was grain motion and rotation observed during terrestrial-based solidification. This can be viewed in the Supplementary video of both sequences available online. This grain motion was largely due to the low density, and thus buoyant,  $\alpha\text{-Al}$  grains coming to rest on the upper surface of the crucible wall, as discussed in the previous work of Murphy et al. [7]. As expected, no such rotation or grain motion was observed during microgravity-based solidification due to the absence of gravity. However, during the latter stages of solidification, when the cooling rate was increased from  $-0.05\ \text{K/s}$  to  $-1\text{--}1.5\ \text{K/s}$ , slight grain motion could be seen in both cases, with grains adjusting position as a result of mechanical impingement, i.e. grains touching one another (coherency), as well as the increased rate of shrinkage-induced liquid feeding as the rate of solid formation increased. Further shrinkage induced grain motion was also apparent during the eutectic transformation, with grains being moved towards the advancing eutectic front(s).

Fig. 5(a) shows the location and sequence of equiaxed nucleation within the FOV for both microgravity (triangles) and terrestrial-based (circles) solidification. Close inspection of Fig. 5(a) reveals a significant overlap of grain locations when comparing both solidification experiments: in particular, Grains 01 and 01, 04 and 14, 11 and 23, 17 and 02, 10 and 15, 02 and 05, 13 and 17, for microgravity and terrestrial solidification, respectively. Furthermore, two relatively large intergranular liquid voids appear in the same location in both experiments, at the W edge of the FOV and to the NE of the centre of the FOV. As mentioned previously, these similar nucleation locations with later/earlier nucleation times may be a result of gravity effects or due to the reorientation of inoculant particles during re-melting of the sample on the microgravity flight. For instance, Grain 01 nucleates in virtually the same location in both experiments, however, nucleating earlier during microgravity. Close examination of Grain 01 in Fig. 4 shows that during microgravity (column I) a more cruciform morphology

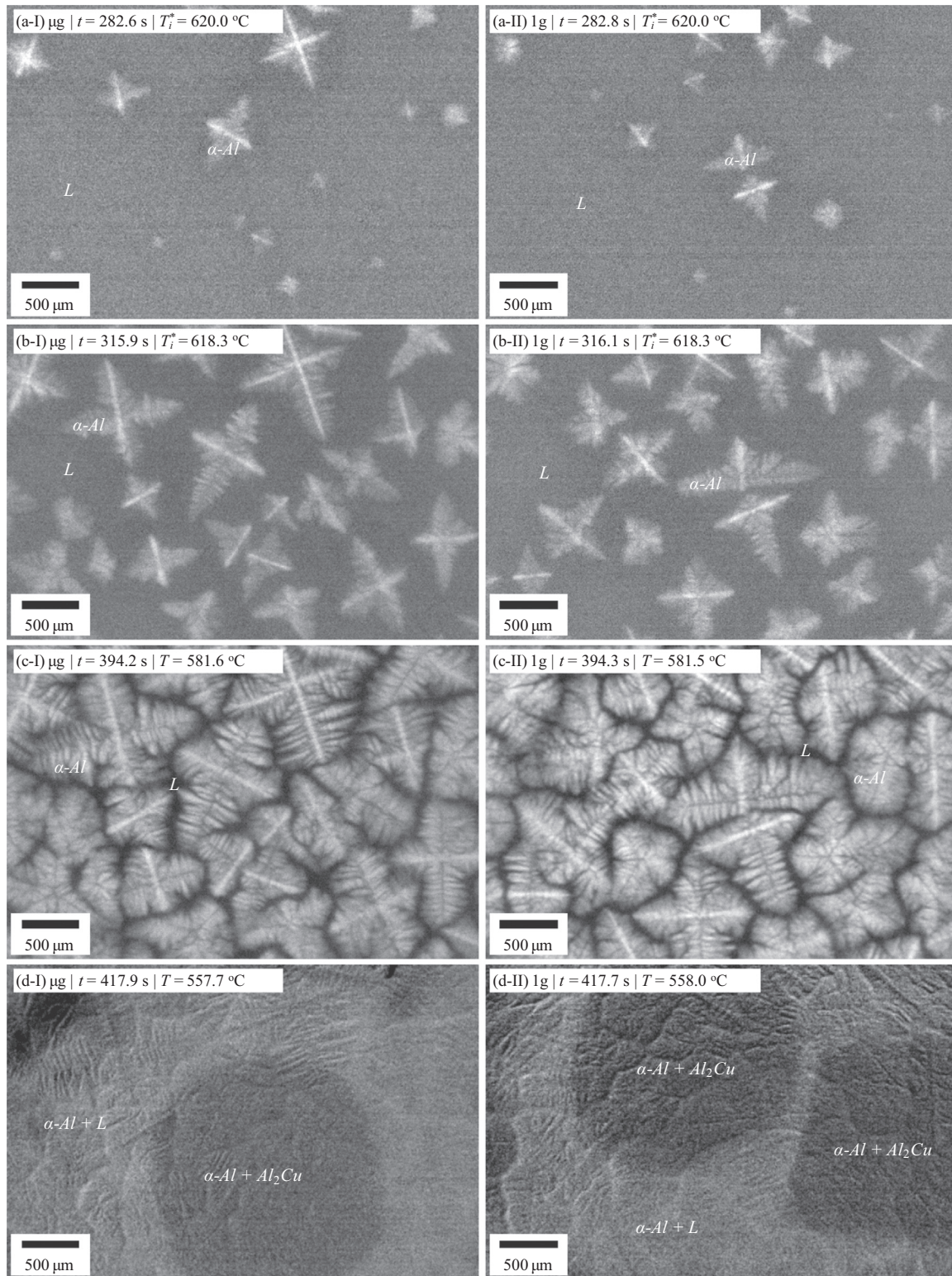


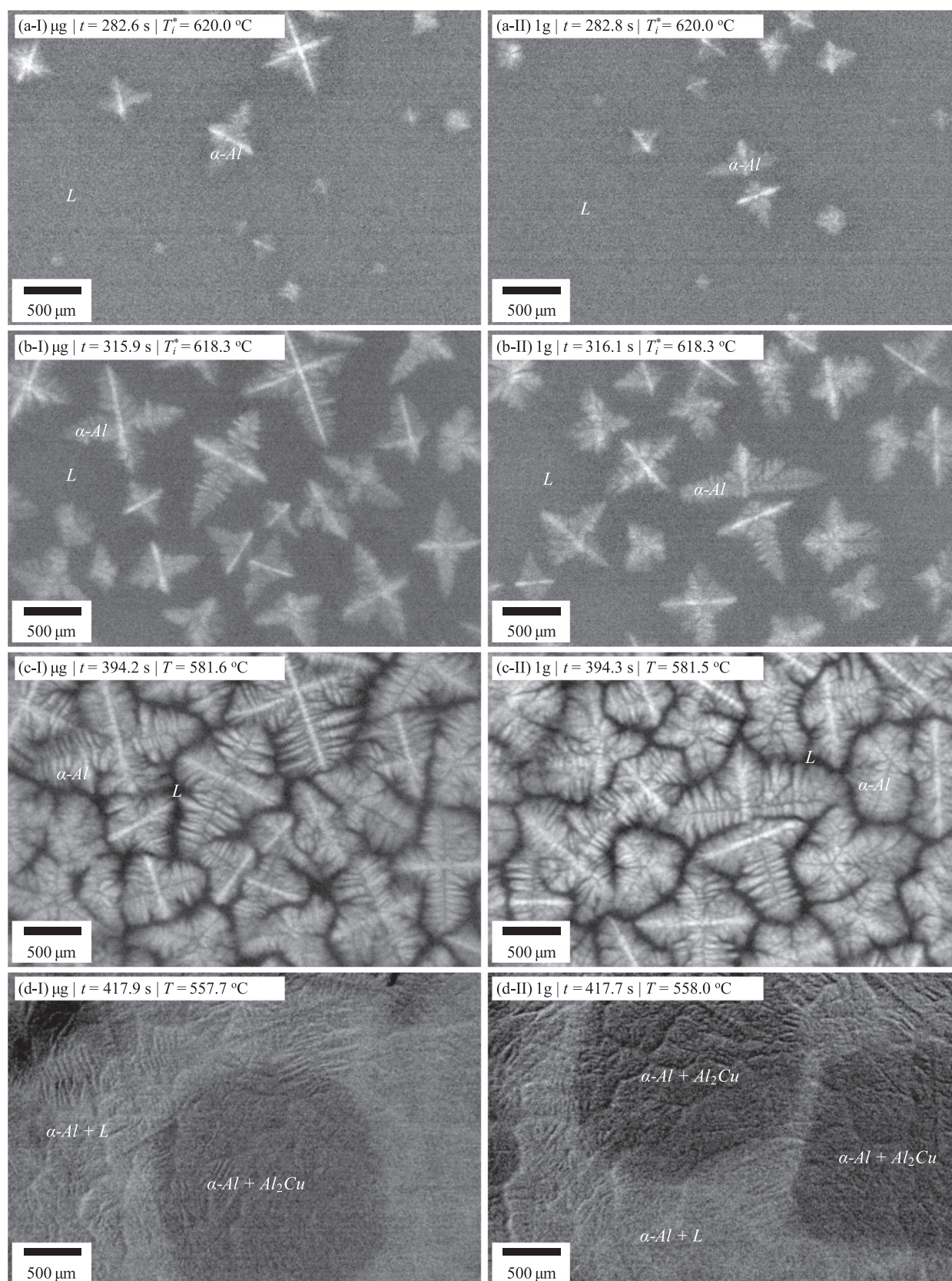
**Fig. 4.** Sequence of images recorded in microgravity ( $\mu\text{g}$ ) on board the MASER 13 Sounding Rocket (column I), alongside ground-based (1g) images (column II) recorded using the same sample, furnace, and experiment timeline. Note, images in row (d) have had the equiaxed grain structure removed, using post-experiment digital image processing, to more clearly show the eutectic transformation [23]. See [Video Sequence 1](#) for both solidification sequences run side-by-side.

was apparent, with the primary dendrite arms aligned favourable in the plane of the FOV, i.e. into the liquid volume, whereas the during terrestrial-based solidification Grain 01 (column II) was misaligned with respect to the FOV suggesting primary growth biased towards the crucible walls, and therefore suppressed.

Differences in nucleation times could also be due to slightly differing thermal contact and furnace environment in 1g vs.  $\mu\text{g}$ .

[Fig. 5\(b\)](#) shows cumulative equiaxed nucleation as a function of furnace temperature for microgravity and terrestrial-based solidification, triangles and circles, respectively. Interestingly, after





**Video 1.** X-ray video sequence of equiaxed solidification, showing evolving time and furnace temperature. Left side: microgravity ( $\sim 0g$ ) conditions; Right side: terrestrial ( $1g$ ) conditions. Corresponding still images, at 4 selected times, are shown in Fig. 4. A video clip is available online. Supplementary material related to this article can be found online at <http://dx.doi.org/10.1016/j.jcrysgro.2016.08.054>.

**Table 1**

Temporospatial coordinates of the 22 equiaxed nucleation events occurring within the in situ FOV recorded on board the MASER 13 Sounding Rocket flight during microgravity. Note, recorded nucleation temperatures represent the indicated furnace temperature at the time when respective grains first became visible within the FOV. Grain #3 highlighted for growth analysis shown in Fig. 6(a).

Grain	<i>x</i> (μm)	<i>y</i> (μm)	<i>t</i> (s)	<i>T</i> (°C)	Grain	<i>x</i> (μm)	<i>y</i> (μm)	<i>t</i> (s)	<i>T</i> (°C)
1	160.92	2301.40	241.31	622.09	12	2728.14	1208.64	279.95	620.15
2	2541.02	2406.18	249.64	621.70	13	3229.61	482.64	280.28	620.13
3	1942.25	1627.78	262.30	621.04	14	2024.59	849.38	280.28	620.13
4	991.71	1934.65	270.63	620.60	15	1328.52	662.27	281.28	620.06
5	3656.23	2660.66	271.96	620.54	16	3828.37	841.90	282.95	619.98
6	1650.36	2638.20	272.62	620.51	17	2376.36	1133.80	282.95	619.98
7	3925.67	1784.96	273.62	620.45	18	3049.98	1448.15	283.62	619.95
8	2466.18	295.52	276.95	620.29	19	1687.78	243.13	287.61	619.74
9	2234.15	684.72	277.95	620.24	20	819.56	669.75	289.94	619.63
10	3514.02	1814.90	278.62	620.20	21	1186.31	1253.55	292.28	619.51
11	437.85	557.48	279.62	620.17	22	580.06	939.20	292.61	619.49

**Table 2**

Temporospatial coordinates of the 23 equiaxed nucleation events occurring within the in situ FOV recorded during ground-based reference solidification experiment prior to the MASER 13 Sounding Rocket flight. Note, recorded nucleation temperatures represent the indicated furnace temperature at the time when respective grains first became visible within the FOV. Grain #2 highlighted for growth analysis shown in Fig. 6(b).

Grain	<i>x</i> (μm)	<i>y</i> (μm)	<i>t</i> (s)	<i>T</i> (°C)	Grain	<i>x</i> (μm)	<i>y</i> (μm)	<i>t</i> (s)	<i>T</i> (°C)
1	160.92	2428.63	254.11	621.46	13	2675.75	48.53	280.10	620.12
2	2346.42	1126.31	259.11	621.19	14	999.19	1949.62	281.43	620.06
3	2234.15	1365.82	262.44	621.04	15	3543.96	1777.47	282.76	620.00
4	2735.62	2690.60	265.77	620.87	16	1365.94	2308.88	283.43	619.96
5	2503.60	2466.06	266.11	620.85	17	3207.15	467.67	284.76	619.90
6	3020.04	2346.30	267.11	620.79	18	782.14	961.65	287.42	619.77
7	1942.25	2443.60	272.77	620.49	19	4090.34	205.71	288.42	619.71
8	2997.58	909.26	273.10	620.48	20	3716.11	2413.67	288.76	619.69
9	1358.46	1590.36	273.43	620.49	21	1380.91	886.81	290.42	619.60
10	3955.61	1814.90	277.43	620.27	22	3925.67	520.06	291.42	619.57
11	1837.47	2106.80	278.10	620.22	23	407.91	550.00	294.75	619.37
12	1874.89	370.37	280.10	620.12	-	-	-	-	-

two or three grains had nucleated in each case, the nucleation rates were somewhat comparable for the remainder of solidification, i.e.  $16.7\text{ }^{\circ}\text{C}^{-1}$  and  $14.8\text{ }^{\circ}\text{C}^{-1}$ , respectively, with the rate of nucleation slightly higher during microgravity.

Using the image analysis technique described by Murphy et al. [7], the 2D solid fraction evolution,  $f_v$ , was extracted from both microgravity ( $\mu\text{g}$ ) and terrestrial ( $1\text{g}$ ) solidification, as shown in Fig. 5(c), for solidification time  $t=240\text{--}359\text{ s}$ , when primary equiaxed growth had slowed to a visually imperceptible level. Further evidence of equiaxed growth suppression is evident when comparing both curves, with a higher fraction of solid apparent during the mid stages of microgravity-based solidification. However, at the end of primary equiaxed growth ( $t=360\text{ s}$ ), the apparent fraction of solid in both cases had equalised.

Fig. 6 shows the primary equiaxed growth profiles extracted from microgravity (row-i) and terrestrial-based (row-ii) solidification, respectively. In each case, a single equiaxed grain exhibiting a distinctly cruciform morphology, and close to the centre of the FOV, was selected for characterisation, Grains 03 and 02 in Fig. 6(a-i) and (a-ii), respectively. The evolution of each of the primary arm lengths over time is shown in Fig. 6(b-i) and (b-ii). Interestingly, there was little difference between the growth profiles measured for both microgravity and terrestrial solidification, with each of the four primary branches showing similar growth rates and final lengths. The only significant difference being, during terrestrial solidification (row-ii), Grains 02 and 03 nucleated quite close to each other thereby restricting the growth of both dendrite arms in the direction of the grain separation spacing. Consequently, the similar growth characteristics of microgravity

and terrestrial solidification suggest that early grain motion and rotation observed during terrestrial solidification had little impact on the resultant growth dynamics during the remainder of solidification. The similarity of both microgravity and terrestrial solidification in this case is likely due to the dominance of solutal redistribution throughout the sample in the absence, in the case of microgravity solidification, or with limited, in the case of terrestrial solidification, liquid motion as a result of using a high-solute alloy sample combined with a relatively high grain density. Thus, a lower solute Al–Cu alloy, combined with a lower inoculant addition level, may result in more obvious differences between terrestrial and microgravity solidification. A more detailed analysis of dendrite growth rates in multiple equiaxed grains solidified in  $1\text{g}$  in XRMON-SOL has previously been performed [8].

#### 4. Conclusions

A first ever space experiment in which the entire equiaxed solidification sequence of a metallic alloy in microgravity has been directly observed by X-ray videography has been performed.

Comparisons of microgravity and terrestrial solidification showed little difference in terms of grain density, growth characteristics, undercooling at which primary growth slowed to visually imperceptible levels, and eutectic transformation. Thus, under terrestrial conditions, where equiaxed buoyancy and liquid motion have been effectively limited [7,8], conditions are sufficiently similar to microgravity conditions. However, the results pertain specifically to those conditions examined in this work.



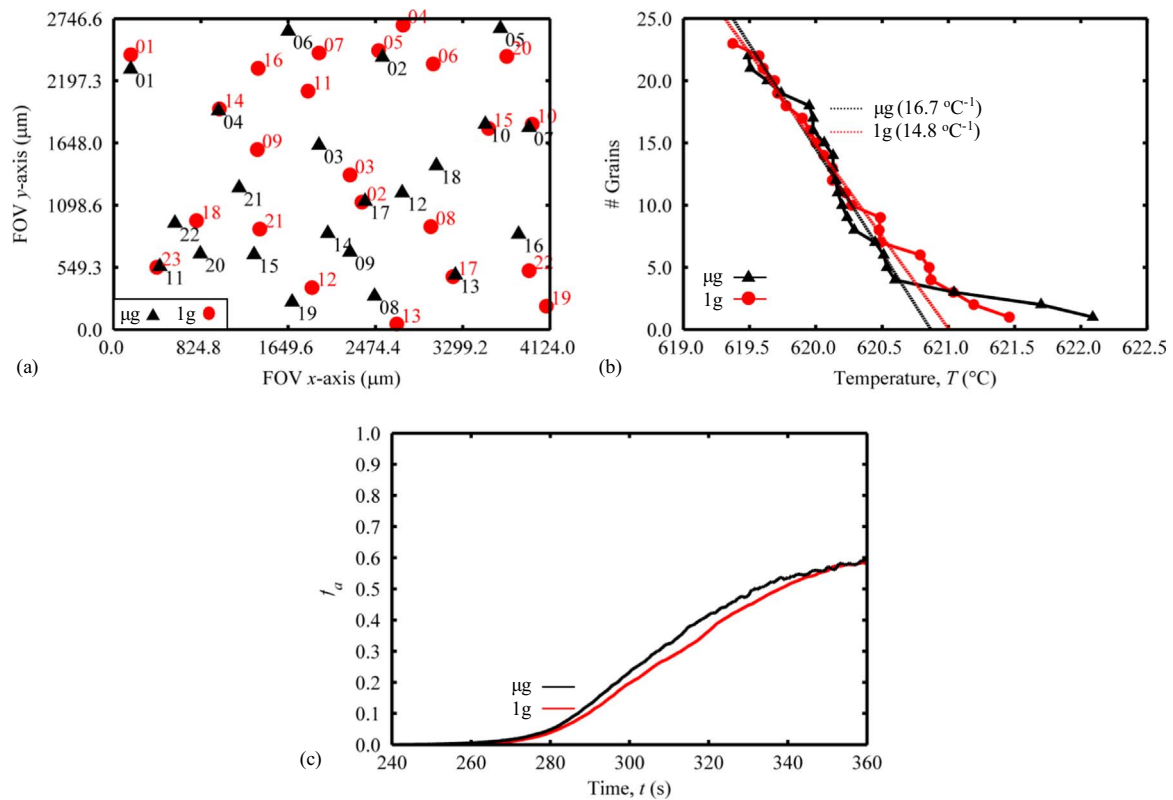


**Fig. 5.** (a) Location and sequence of equiaxed nucleation events recorded in situ on board the MASER 13 Sounding Rocket ( $\mu\text{g}$  ▲) and during the ground-based reference experiment performed prior to launch (1g ●). (b) A comparison of microgravity and terrestrial equiaxed nucleation events as a function of recorded furnace temperature ( $T$ ). (c) Equiaxed grain area envelope evolution ( $f_a$ ) as a function of time ( $t$ ) for both microgravity ( $\mu\text{g}$ ) and terrestrial (1g) solidification experiments, recorded during primary equiaxed growth phase of solidification, i.e.  $240 \leq t \leq 360$  s of the experiment timeline.

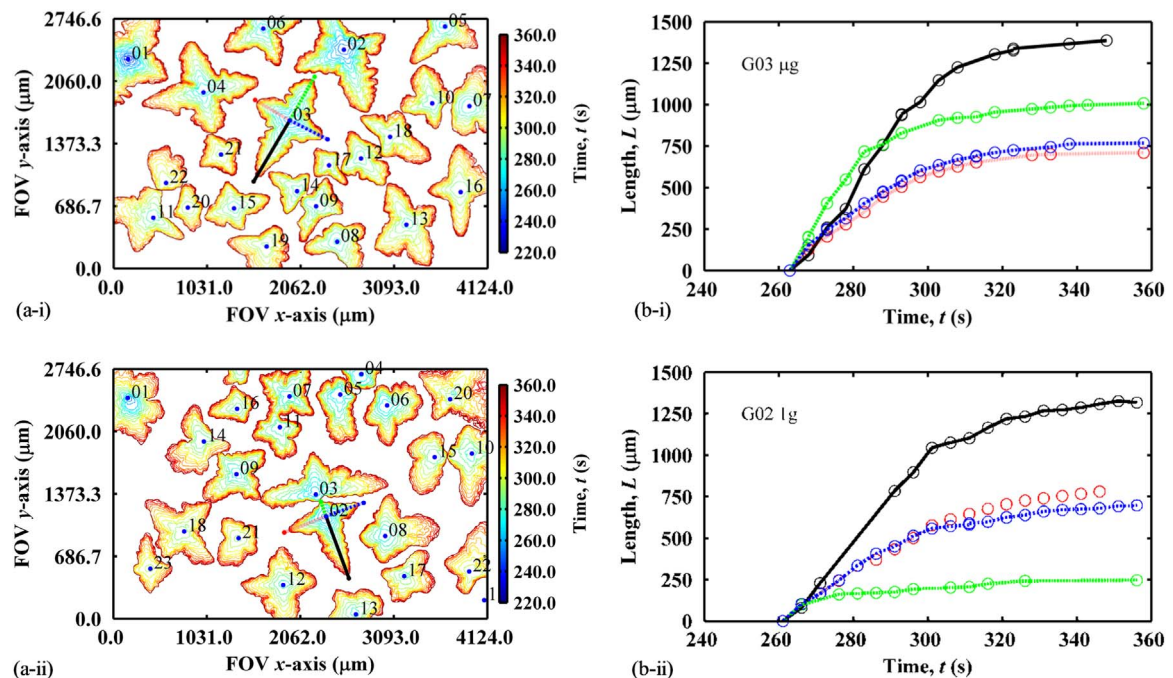


**Fig. 6.** (a-i) Equiaxed grain envelope evolution recorded as a function of time ( $t$ ) across the in situ FOV for the microgravity ( $\mu\text{g}$ ) solidification experiment timeline. (b-i) Primary arm growth as a function of time ( $t$ ) for Grain G03 (Fig. 6(a-i)). (a-ii) Equiaxed grain envelope evolution recorded as a function of time ( $t$ ) across the in situ FOV for the terrestrial (1g) solidification experiment timeline. (b-ii) Primary arm growth as a function of time ( $t$ ) for Grain G02 (Fig. 6(a-ii)). In both cases, the colour scales to the right of the FOVs represent the experiment timeline period  $240 \leq t \leq 260$  s.

Nguyen-Thi et al. [12] observed a reduction in growth rate during columnar solidification using the same X-ray diagnostics and a gradient furnace (XMON-GF). Where samples have larger volumes

with an aspect ratio closer to 1, it is certain that a significant disparity between microgravity and terrestrial solidification exists.

While grain rotation is prevalent during the early post-

nucleation stages of solidification during terrestrial-based solidification, this had no significant impact on the resultant equiaxed solidification, and the final as-cast microstructure. By contrast, no such grain rotation was observed in the early stages of solidification in microgravity. During the latter stages of solidification, when the cooling rate had been increased two orders of magnitude, grain motion could be seen in both cases as a result of increased shrinkage-induced liquid feeding. Thus it seems reasonable, in this case, to assume solidification performed under terrestrial conditions using the horizontal thin sample configuration adequately simulates microgravity conditions during solidification. However, here we present unique benchmark data on equiaxed solidification of metallic alloys in space, in which gravity effects are neither visible nor expected. These results may be useful for experimental validation of computational models of microstructural evolution, and also isolate shrinkage-induced motion of equiaxed grains.

## Acknowledgements

The authors wish to acknowledge the financial support of the European Space Agency (ESA) under the PRODEX program, (contract numbers 90392 and 4000110414). This work is part of the ESA-MAP (Microgravity Applications Promotion) project XRMON. The space hardware and XRMON-SOL furnace development was funded through ESA's ELIPS (European Life and Physical Sciences in Space) programme.

## References

- [1] J. Campbell, Castings, Butterworth-Heinemann, Oxford, UK, 1991.
- [2] V.R. Voller, F. Porté-Agel, Moore's law and numerical modeling, *J. Comput. Phys.* 179 (2) (2002) 698–703.
- [3] R. Mathiesen, L. Arnberg, H. Nguyen-Thi, B. Billia, *In situ* X-ray video microscopy as a tool in solidification science, *JOM* 64 (1) (2012) 76–82.
- [4] H. Nguyen-Thi, L. Salvo, R.H. Mathiesen, L. Arnberg, B. Billia, M. Suery, G. Reinhart, On the interest of synchrotron X-ray imaging for the study of solidification in metallic alloys, *Comptes Rendus Phys.* 13 (3) (2012) 237–245.
- [5] A.G. Murphy, G. Reinhart, H. Nguyen-Thi, G. Salloum Abou Jaoude, D.J. Browne, Meso-scale modelling of directional solidification and comparison with *in situ* X-ray radiographic observations made during the MASER-12 XRMON microgravity experiment, *J. Alloy. Compd.* 573 (2013) 170–176.
- [6] D.R. Liu, G. Reinhart, N. Mangelinck-Noel, C.-A. Gandin, H. Nguyen-Thi, B. Billia, Coupled Cellular Automaton (CA) – Finite Element (FE) modeling of directional solidification of Al–3.5 wt%Ni alloy: a comparison with X-ray synchrotron observations, *ISIJ Int* 54 (2) (2014) 392–400.
- [7] A.G. Murphy, W.U. Mirihanage, D.J. Browne, R.H. Mathiesen, Equiaxed dendritic solidification and grain refiner potency characterised through *In Situ* X-radiography, *Acta Mater.* 95 (2015) 83–89.
- [8] A.G. Murphy, R.H. Mathiesen, Y. Houlitz, J. Li, C. Lockowandt, K. Henriksson, G. Zimmermann, N. Melville, D.J. Browne, XRMON-SOL: isothermal equiaxed solidification of a grain refined Al–20 wt%Cu alloy, *J. Cryst. Growth* 440 (2016) 38–46.
- [9] A. Bogno, H. Nguyen-Thi, G. Reinhart, B. Billia, J. Baruchel, Growth and interaction of dendritic equiaxed grains: *in situ* characterization by synchrotron X-ray radiography, *Acta Mater.* 61 (4) (2013) 1303–1315.
- [10] S. McFadden, P.L. Schaffer, R.H. Mathiesen, D.J. Browne, Analysis of an equiaxed dendrite growth model with comparisons to *in situ* results of equiaxed dendritic growth in an Al–Ge alloy, *Mater. Sci. Forum* 654–656 (2010) 1359–1362.
- [11] C. Rakete, C. Baumbach, A. Goldschmidt, D. Samberg, C.G. Schroer, F. Breede, C. Stenzel, G. Zimmermann, C. Pickmann, Y. Houlitz, C. Lockowandt, O. Svenonius, P. Wiklund, R.H. Mathiesen, Compact X-ray microradiograph for *in situ* imaging of solidification processes: bringing *In situ* X-ray micro-imaging from the synchrotron to the laboratory, *Rev. Sci. Instrum.* 82 (10) (2011), pp. 105108–105108–10.
- [12] H. Nguyen-Thi, G. Reinhart, G. Salloum Abou Jaoude, R.H. Mathiesen, G. Zimmermann, Y. Houlitz, D. Voss, A. Verga, D.J. Browne, A.G. Murphy, XRMON-GF: a novel facility for solidification of metallic alloys with *in situ* and time-resolved X-ray radiographic characterization in microgravity conditions, *J. Cryst. Growth* 374 (2013) 23–30.
- [13] M. Becker, C. Dreißigacker, S. Klein, F. Kargl, Near-isothermal furnace for *in situ* and real time X-ray radiography solidification experiments, *Rev. Sci. Instrum.* 86 (6) (2015) 063904.
- [14] A.G. Murphy, J. Li, O. Janson, A. Verga, D.J. Browne, Microgravity and hypergravity observations of equiaxed solidification of Al–Cu alloys using *in-situ* X-radiography recorded in real-time on board a parabolic flight, *Mater. Sci. Forum* 790–791 (2014) 52–58.
- [15] M.E. Glicksman, M.B. Koss, E.A. Winsa, Dendritic growth velocities in microgravity, *Phys. Rev. Lett.* 73 (4) (1994) 573–576.
- [16] B.K. Dhindaw, D.M. Stefanescu, A.K. Singh, P.A. Curreri, Directional solidification of Cu–Pb and Bi–Ga monotectic alloys under normal gravity and during parabolic flight, *Met. Trans. A* 19 (11) (1988) 2839–2846.
- [17] L. Sturz, G. Zimmermann, Microgravity experiments on columnar–equiaxed transition in Al based alloys, *Int. J. Cast. Met. Res.* vol. 20 (3) (2007) 122–126.
- [18] W.U. Mirihanage, D.J. Browne, G. Zimmermann, L. Sturz, Simulation of international space station microgravity directional solidification experiments on columnar-to-equiaxed transition, *Acta Mater.* 60 (18) (2012) 6362–6371.
- [19] H. Nguyen-Thi, G. Reinhart, G. Salloum-Abou-Jaoude, D.J. Browne, A. G. Murphy, Y. Houlitz, J. Li, D. Voss, A. Verga, R.H. Mathiesen, G. Zimmermann, XRMON-GF experiments devoted to the *in situ* X-ray radiographic observation of growth process in microgravity conditions, *Microgravity Sci. Technol.* 26 (2014) 37–50.
- [20] V. Pletzer, S. Rouquette, U. Friedrich, J.-F. Clervoy, T. Gharib, F. Gai, C. Mora, European parabolic flight campaigns with Airbus ZERO-G: looking back at the A300 and looking forward to the A310, *Adv. Space Res.* 56 (2015) 1003–1013.
- [21] R.H. Mathiesen, L. Arnberg, K. Ramsøskar, T. Weitkamp, C. Rau, A. Snigirev, Time-resolved X-ray imaging of aluminium alloy solidification processes, *Met. Mater. Trans. B* 33 (4) (2002) 613–623.
- [22] A.G. Murphy, *In Situ* X-Ray Monitoring of Advanced Alloy Solidification Processes under Microgravity and Terrestrial Conditions (PhD Thesis), University College Dublin, Ireland, 2013.
- [23] A.G. Murphy, D.J. Browne, W.U. Mirihanage, R.H. Mathiesen, Combined *in situ* X-ray radiographic observations and post-solidification metallographic characterisation of eutectic transformations in Al–Cu alloy systems, *Acta Mater.* 61 (12) (2013) 4559–4571.